Diagnostic and Interventional Imaging 104 (2023) 167–177



Review/*Research, New developments & Artificial Intelligence*

Spectral CT imaging: Technical principles of dual-energy CT and multi-energy photon-counting CT



Joël Greffier[a,b,*], Nicolas Villani[a,c], Didier Defez[a,d], Djamel Dabli[a,b], Salim Si-Mohamed[a,e,f]

[a] *Groupe de travail – Imagerie Spectrale, Société Française de Radiologie (SFR), Société Française de Physique Médicale (SFPM), G4, Collège des Enseignements de la Radiologie Française (CERF), 75013 Paris, France*
[b] *Department of Medical Imaging, CHU Nimes, Univ Montpellier, Nîmes Medical Imaging Group, EA 2992, 30029 Nîmes, France*
[c] *Radioprotection Unit, Central Hospital, University Hospital Center of Nancy, 54035 Nancy, France*
[d] *Department of Medical Physics and Radioprotection, Hopital Lyon Sud, Hospices Civils de Lyon, 69495 Pierre Benite, France*
[e] *University of Lyon, INSA-Lyon, University Claude Bernard Lyon 1, UJM-Saint Etienne, CNRS, Inserm, CREATIS UMR 5220, U1206, 69621, Villeurbanne, France*
[f] *Department of Radiology, Louis Pradel Hospital, Hospices Civils de Lyon, Bron, 69500 France*

A R T I C L E I N F O

Keywords:
Computed tomography
Dual-energy CT
Image quality
Photon-counting CT
Spectral photon-counting CT

A B S T R A C T

Spectral computed tomography (CT) imaging encompasses a unique generation of CT systems based on a simple principle that makes use of the energy-dependent information present in CT images. Over the past two decades this principle has been expanded with the introduction of dual-energy CT systems. The first generation of spectral CT systems, represented either by dual-source or dual-layer technology, opened up a new imaging approach in the radiology community with their ability to overcome the limitations of tissue characterization encountered with conventional CT. Its expansion worldwide can also be considered as an important leverage for the recent groundbreaking technology based on a new chain of detection available on photon counting CT systems, which holds great promise for extending CT towards multi-energy CT imaging. The purpose of this article was to detail the basic principles and techniques of spectral CT with a particular emphasis on the newest technical developments of dual-energy and multi-energy CT systems.
© 2022 The Authors. Published by Elsevier Masson SAS on behalf of Société française de radiologie. This is an open access article under the CC BY-NC-ND license (http://creativecommons.org/licenses/by-nc-nd/4.0/)

1. Introduction

Spectral computed tomography (CT) imaging encompasses a unique generation of CT systems based on a simple principle that makes use of the energy-dependent information present in CT images. Over the past two decades this principle has been expanded with the introduction of dual-energy CT (DECT) systems. The first generation of spectral CT systems, represented either by dual-source or dual-layer technology, opened up a new imaging approach in the radiology community with their ability to overcome the limitations of tissue characterization encountered with conventional CT. Its expansion worldwide can also be considered as an important leverage for the recent groundbreaking technology based on a new chain of detection available on photon counting CT systems, which holds great promise for extending CT towards multi-energy CT imaging.

The purpose of this article was to detail the basic principles and techniques of spectral CT with a particular emphasis on the newest technical developments of DECT and multi-energy CT systems and make the reader more familiar with this technology.

2. Principles and techniques of dual-energy and multi-energy CT technology

2.1. Physical basis

CT imaging is based on measuring the linear absorption coefficients of different tissues an X-ray beam passes through. Each tissue has its own linear absorption coefficient depending on its physical density and atomic number as well as the energy of the beam [1–3]. During the interaction between X-rays and matter, the photons are attenuated by biological media according to an exponential law which is a factor of the photoelectric effect and Compton scattering. In the human body, the X-ray beam passes through an infinite number of tissues with different densities for a given projection, making it extremely difficult to understand the interaction between photons

Abbreviations: ASIC, Application-specific integrated circuit; CNR, Contrast-to-noise ratio; CT, Computed tomography; DECT, Dual-energy CT; DSCT, Dual-source CT; FOV, Field of view; HU, Hounsfield unit; MTF, Modulation transfer function; NPS, Noise power spectrum; PCD, Photon-counting detectors; ROI, Region of interest; SNR, Signal-to-noise ratio; SPCCT, Spectral photon-counting CT; TTF, Task-based transfer function; VMI, Virtual monochromatic image

* Corresponding author.
E-mail address: joel.greffier@chu-nimes.fr (J. Greffier).

https://doi.org/10.1016/j.diii.2022.11.003
2211-5684/© 2022 The Authors. Published by Elsevier Masson SAS on behalf of Société française de radiologie. This is an open access article under the CC BY-NC-ND license (http://creativecommons.org/licenses/by-nc-nd/4.0/)

and matter. To identify the linear attenuation coefficient (μ) of each tissue the beam passes through, multiple projections are therefore performed around an object or patient using helical CT systems. During the reconstruction process, each voxel is assigned to a Hounsfield unit (HU) value based on the μ of the tissue present in it, compared to the μ of the water, taken as a reference.

Using conventional CT, only one X-ray spectrum is used and the attenuation measurement is integrated, consequently losing all the energy dependence of a specific tissue. Unfortunately, for the same X-ray beam's energy, if the μ of two tissues are similar (calcium and bone for example), the same HU value will be assigned to both tissues and it will be difficult to differentiate them. To overcome this limitation, a new field in CT technology termed "spectral CT imaging" has been developed. The general idea is to take advantage of a tissue's energy-dependent data, by mainly measuring and differentiating between tissues based on their weighting photoelectric effect and Compton scattering.

DECT is based on the acquisition or detection of two photon spectra, one high energy and one low energy [4–9]. Alvarez and Macovski [10] defined a formula to calculate the role of the photoelectric effect and the Compton effect in the attenuation coefficient (μ) of tissue for a given energy (E):

$$\mu(E) = \mu_P(E) + \mu_C(E) = \alpha_P f_P(E) + \alpha_C f_c(E) \quad (1)$$

with $f_P(E)$nd $f_C(E)$ two known mathematical functions that depend only on the energy of the photon beam. α_P and α_C are the coefficients describing the contributions of the photoelectric and Compton effects respectively. These values only depend on the tissue's atomic number (Z).

From the two datasets at two different energies obtained at acquisition or detection, it is then possible to solve a system of two equations with two unknowns, α_p and α_c:

$$\mu(LE) = \alpha_P f_P(LE) + \alpha_C f_c(LE) \quad (2)$$

$$\mu(HE) = \alpha_P f_P(HE) + \alpha_C f_c(HE) \quad (3)$$

with $\mu(HE)$ and $\mu(LE)$ the attenuation coefficients for high and low energy X-ray beams.

After solving this system of two equations, each voxel in the image has a pair of values (α_P, α_c). These two values are then recombined to artificially recreate different types of spectral image.

2.2. Spectral image creation

The different types of images generated by DECT platforms are based on a recombination of the values for α_p and α_c of each voxel. This reconstruction can be made in the projection domain or in the image domain depending on the temporal resolution of the technique. Indeed, DECT platforms with good temporal resolution allow reconstruction from raw data in the projection domain. Conversely, the image domain is used for platforms that cannot offer sufficient temporal coherence between the two spectra acquired. This is also called image-based reconstruction. Photoelectric and Compton basis image pairs are processed to generate several types of images.

2.2.1. Material decomposition images

The decomposition of materials is usually based on low and high kVp attenuations of two or three materials like iodine, water and calcium. The characteristics of these basic materials are well-known and used [4,11-13]. Any material can be expressed as a function of HU at low and high kVp so its concentration in the tissues can thus be distinguished and quantified. With this method, several materials present in the tissues (such as iodine, water or calcium) can therefore be identified during examination (Fig. 1). However, it is still difficult to identify and characterize components with very similar HU values like blood and water. The principle of material identification with respect to base materials is depicted in Fig. 1. Each material has a specific position according to these characteristics (Z, attenuation). Therefore, it is possible to identify a material according to its position in relation to basic materials. The slope of the curve characterizes a material with different concentrations (*e.g.*, iodine or calcium) and the position of the material on the curve is itself dependent on its concentration [14–19].

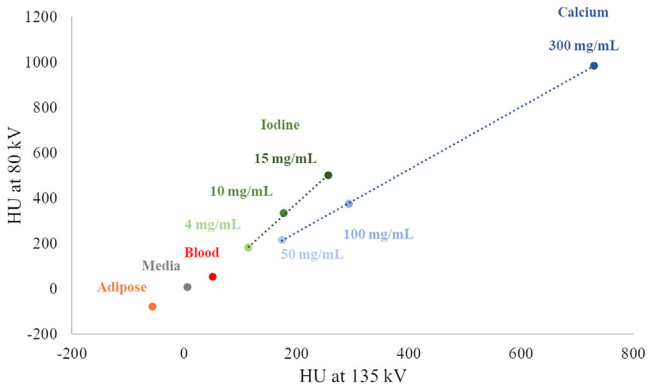


Fig. 1. Example of a geometrical illustration of material decomposition process in different materials based on their absorption linear coefficient (CT attenuation) at low and high energies. Data were acquired on a multi-energy CT phantom (Gammex™ Technology) with a Aquilion ONE system (Canon Medical Systems).

Decomposition of materials makes it possible to generate images virtually, without bone (virtual non calcium) for bone marrow edema assessment [20,21] or iodine (virtual non contrast or virtual unenhanced images) for substitution of a non-contrast phase [22,23] or, on the contrary, with enhanced contrast with a kind of overlay of iodine on images (iodine map imaging) (Fig. 2) [31,32]. On the iodine map, iodine concentration can be measured in lesions for tumor staging and characterizations or any organ by assessing its perfusion [24–34]. These specific material images are used in other clinical applications, for example, to identify uric acid in gout [35–37] or to characterize kidney stones [38–41].

Material image maps can also be used for treatment in radiation therapy [42,43]. The use of DECT to generate electron density maps relative to water and the effective atomic number (Z effective image) improve the stopping power ratio prediction for the dose calculation compared to the single-energy CT technique [44,45]. For photon therapy, the main advantage is to improve contouring of the organ at risk and target volumes, by using iodine subtraction, particularly in treatment planning, when large vessels such as in the heart or bladder are injected for high contrast enhancement [46–48].

2.2.2. Virtual monochromatic images (VMIs)

Virtual monochromatic images (VMIs) simulate the appearance of images obtained with a monochromatic X-ray source. They are generated by a process equivalent to that of the decomposition of materials using the contribution of the photoelectric and Compton effect:

$$\mu(E_m) = \left(\rho_p\right).f_p(E_m) + \left(\rho_c\right).f_C(E_m) \quad (4)$$

where $f_p(E_m)$ and $f_C(E_m)$ are functions that depend on the photoelectric and Compton effects and ρ_p and ρ_c are the mass densities obtained during decomposition of materials. The density values of each pixel are then converted into monochromatic virtual images and generate images at a single keV.

In practice, systems offer a wide range of energy levels, from 35 to 200 keV according to the DECT platform. Depending on the clinical application, these images improve the contrast-to-noise ratio (CNR) by using low energy level values (40 to 70 keV) enabling the reduction in contrast agent volume [49,50] and reduce image artefacts (beam-hardening, blooming) with high energy level values [49,51-53].

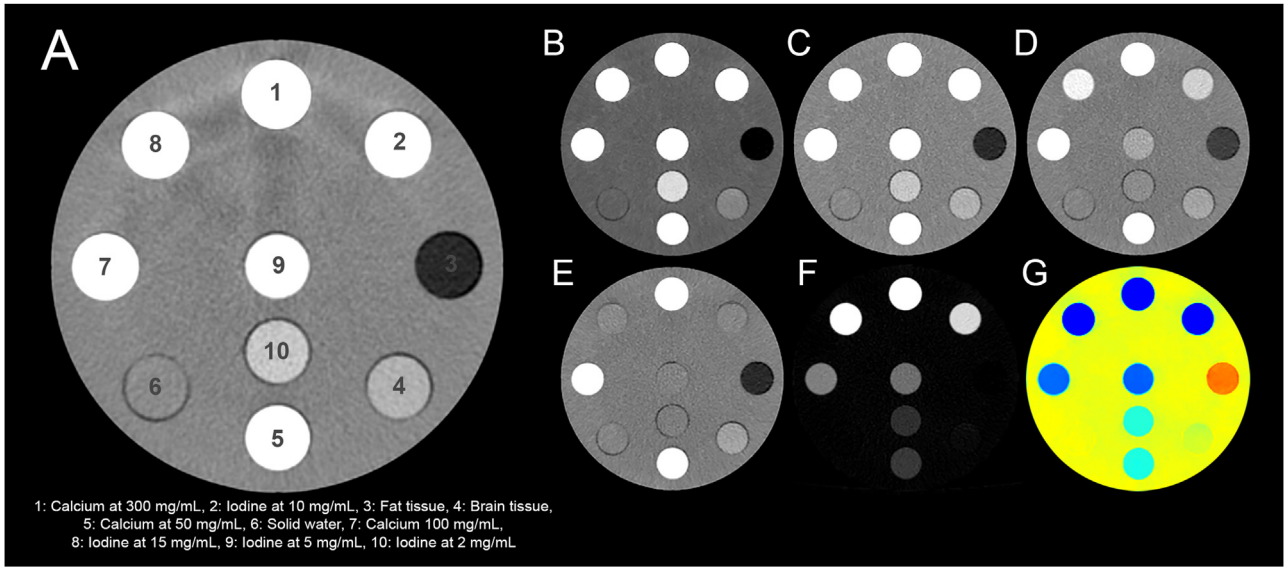


Fig. 2. Illustration of the spectral dual-energy CT capabilities available on all the current dual energy CT platforms.
A, Conventional image of the multi-energy CT phantom (Gammex^{TM} Technology) showing 10 inserts made of different tissue from which their characterization will be revealed using the spectral images.
B, C, D, Virtual monochromatic images at 40, 70 and 135 keV, respectively, that show the iodine boost expected from both calcium and iodine at low keV.
E, Virtual non contrast image that simulates a conventional image without the iodine component. This explains the low density for iodinated inserts numbered 2, 8, 9 and 10.
F, Iodine image that shows the iodine component in the iodinated inserts numbered 2, 8, 9 and 10. Due to the limitation of a material decomposition into only two energies, the calcium components found in the inserts numbered 1, 5 and 7 are noticeable in the iodine images.
G, Z-effective image that measures the average atomic number of a tissue. This map allows new contrast in CT such as observable with the insert numbered 3 that is made of fat tissue (*i.e.*, a low atomic number).

2.3. Technological aspects of dual-energy CT platforms

Several DECT platforms are available to generate or detect the two photon spectra at high and low energy. Techniques and spectral performances differ, and various types of spectral images are available depending on manufacturers (Table 1).

2.3.1. Canon Medical Systems

For Canon Medical Systems, the two photon spectra are obtained from three different spectral acquisition techniques for five CT systems. Acquisition and reconstruction parameters depend on the CT system and are detailed in Table 2.

The rotate-rotate axial kVp-switching (Dual-energy rotate-rotate) mode consists of performing one rotation on a volume with low tube voltage (80 or 100 kVp) and then another rotation on the same volume with high tube voltage (135 kVp). Between these two rotations, another rotation is performed without X-ray emission to let the CT system invert the two voltage tubes. The two acquisitions are performed on the same axial volume between 40 and 160 mm depending on the CT system. With this acquisition mode, the tube current modulation system can be used. The process of material decomposition is performed on the raw data and the VMI energy levels range from 35 to 135 keV.

In helical kVp-switching (dual-energy helical) mode, the acquisition is performed in helical mode by alternating the kVp (80 or 100 kVp and 135 kVp) at each rotation. For this purpose, the projections are acquired over 360° with a switching time of 0.1 to 0.2 s. There is a partial scan mode for dose reduction purposes that limits direct irradiation of radiosensitive organs. This mode cuts the X-rays when the tube is around zero position with a no-exposure period before reaching 0° and an identical period after 0°. The table moves slowly with each rotation and a low pitch factor is automatically set by the CT system according to the rotation time. With this acquisition mode, the tube current modulation system cannot be used. The process of material decomposition is performed in the image domain and the energy levels of the VMIs with energy ranging from 80 to 135 kVp.

Rapid kVp-switching consists of quickly and repeatedly switching (<1 ms) from high (135 kVp) to low kVp (80 kVp) as the tube detector rotates around the patient. During rotation, the rotation time (or the number of projections) is divided into two equal parts between the two voltage tubes. This tube potential switching provides data acquisition from two different energy spectra, closely aligned, temporally and spatially. Spectral reconstruction works by transforming views acquired with one energy into the other to create deep learning views using a trained deep neural network. Deep learning spectral acquisition mode is available only with the Aquilion ONE Prism CT system. Rapid kVp-switching can be carried out in helical (with a pitch between 0.5 and 1.5 and beam collimations of 40 and 80 mm) or axial (with volumes of 40 and 160 mm) acquisitions. The tube current modulation system and the cardiac mode with gating can be used. The process of material decomposition is performed in the raw data domain itself rather than post-reconstruction in the image domain. This is because raw data-based decomposition has been demonstrated to be less impacted by beam-hardening and other biases that occur when material decomposition is performed in the image domain. The energy levels of the VMIs provide gray scale images in any of 101 energy levels ranging from 35 to 200 keV.

For all acquisition modes, the smallest reconstruction slice thickness available is 0.5 mm, with a reconstruction field of view (FOV) of up to 50 cm and 512^2 pixels matrix size. The iterative reconstruction algorithm AIDR 3D is available for all CT systems, except for the Aquilion ONE Prism. For this system, the deep learning spectral reconstruction algorithm is available [54].

The different types of spectral images generated on the Canon DECT systems are described in Table 1.

2.3.2. GE Healthcare

With GE Healthcare, ultra-fast kVp-switching is available on four CT systems (Table 3). The principle of ultra-fast kVp-switching has already been described in previous studies [55–61]. It consists of quickly switching from 80 kVp to 140 kVp, which is needed to maintain sufficient energy separation between the two spectra. Fast kVp-

Table 1
Different types of spectral images available on the different dual-energy CT platforms.

Image purpose	Canon	GE	Philips	Siemens
Simulate attenuation at a chosen single energy	Virtual monochromatic images (35 to 135 keV or 200 keV*)	Monochromatic images (40 to 140 keV)	Monoenergetic (40 to 200 keV)	Monoenergetic images (40 to 190 keV)
Simulate a non-contrast phase generated from a contrast acquisition	Virtual non-contrast image	Virtual unenhanced image	Virtual non-contrast image	Virtual non-contrast image
Iodine content material decomposition	Iodine map image	Material decomposition	Iodine no water	Iodine map image
Iodine content material suppression	–	Materiel supressed iodine (MSI)	Iodine density	–
Material characterization (Z effective)	Z effective image	Effective Z	Z effective	DE Rho/z
Material characterization (Electron density)	Electron density image	–	Electron density	DE Rho/z
Calcium content material decomposition	Ca/H2O and H2O/Ca images	Material decomposition	Calcium suppression	Bone marrow image
Uric acid content material decomposition	Uric acid curve	Material decomposition	Uric acid	DE gout image
Liver fat content material decomposition	–	GSI Fat	–	Liver VNC/ Fat map image

* Only available on the Aquilion One Prism.
For GE dual-energy CT platforms, material decomposition of different elements is available, allowing different types of spectral images to be created.
GSI: Gemstome spectral imaging; VNC: Virtual noncontrast.

Table 2
Main characteristics of dual-energy CT platforms of Canon Medical Systems.

Model	Aquilion One Prism	Aquilion One Genesis	Aquilion Prime SP	Aquilion Exceed LB	Aquilion Lightning SP
DECT platform	Rapid kVp Switching	Rotate -rotate axial or Helical kVp switching	Helical kVp switching	Rotate-Rotate Axial or Helical kVp switching	Helical kVp switching
kVp available	80/135	80/135; 100/135	80/135; 100/135	80/135; 100/135	80/135; 100/135
Total filtration (eq mmAl)*	11.7 mm*	11.7 mm*	11.7 mm*	11.7 mm*	8.35 mm*
mA range	from 230 to 650	from 50 to 570	from 50 to 570	from 50 to 570	from 50 to 420
TCM system used	SureExposure 3D	SureExposure 3D	No	No	No
Beam collimation range (mm)	Volume: from 40 to 160 & Helical: from 40 to 80	Volume: from 40 to 160 & Helical: from 40 to 80	Helical: 40	Axial & Helical: 40	Helical: 40
Rotation time range (s)	from 0.275 to 1	from 0.275 to 1	from 0.35 to 1	from 0.5 to 1	from 0.35 to 1
Pitch range	from 0.5 to 5	Volume: no pitch & Helical: Automatic pitch	Automatic pitch	Volume: no pitch & Helical: Automatic pitch	Automatic pitch
Temporal resolution max (ms)	137	137	175	250	175
Cardiac gating	Yes	No	No	No	No
Raw data or images space	Raw data	Raw data or images	Images	Raw data or images	Images
Reconstruction algorithm	DLSR	AIDR 3D	AIDR 3D	AIDR 3D	AIDR 3D

* At 120 kVp and large body scan field of view.
AIDR3D: Three-dimensional adaptive iterative dose reduction; DECT: Dual-energy CT; DLSR: Deep learning spectral reconstruction; TCM: Tube current modulation.

switching provides almost simultaneous spatial and temporal registration of projections. Consequently, the spectral data can be processed in the raw data domain.

This switching takes 0.5 ms on the Revolution GSI, and 0.25 ms with other CT systems. While the mA is fixed on most CT systems, the Quantix tube of the Revolution Apex platform provides synchronized kVp and mA switching. This mA switching per kVp improves the image quality (over 10% noise reduction) at low kVp and iodine maps [62]. With the Revolution CT and Revolution Apex platforms, a 3D collimator is added (post patient) to reduce scattering and beam-hardening compared to the classic 1D collimator. kVp-switching can be carried out in helical mode with a pitch factor ranging from 0.5 to 1.5 and in axial mode but only for a volume of 40 mm. In helical mode, a beam collimation of 20 and 40 mm can be used for Revolution GSI and Revolution Frontier and a beam collimation of 40 and 80 mm for Revolution CT and Revolution Apex platforms. Cardiac gating (Smart Cardiac) is possible for GSI acquisitions only on the Revolution GSI and Revolution Frontier.

Table 3
Main characteristics of dual-energy CT platforms of GE Healthcare.

Model	Revolution GSI	Revolution Frontier	Revolution CT & CT ES	APEX platform
DECT platform	Ultrafast kVp Switching (GSI)	Ultrafast kVp Switching (GSI Pro)	Ultrafast kVp Switching (DL Xtream GSI)	Ultrafast kVp Switching (DL Xtream GSI with Quantix tube)
kVp available	80/140	80/140	80/140	80/140
Total filtration (eq mmAl)*	8.4 mm*	8.4 mm*	8.5 mm*	8.3 mm*
mA range	5–765	5–765	5–735	5–630
TCM system used	No	No	No	mA switching
Beam collimation range (mm)	20 & 40	20 & 40	from 5 to 80	from 5 to 80
Rotation time range (s)	from 0.5 to 1	from 0.5 to 1	from 0.28 to 1	from 0.28 to 1
Pitch range	from 0.531 to 1.531	from 0.531 to 1.531	from 0.508 to 1.531	from 0.508 to 1.531
Cardiac gating	Yes	Yes	WIP GSI	WIP GSI
Raw data or images space	Raw data	Raw data	Raw data	Raw data
Reconstruction algorithm	ASIR	ASIR-V	ASIR-V & TrueFidelity™	ASIR-V & TrueFidelity™

* At 140 kVp and large body scan field of view.
ASIR: Adaptive statistical iterative reconstruction: DECT: Dual-energy CT; DL: Deep-learning; GSI: Gemstone spectral imaging; TCM: Tube current modulation; WIP: Work in progress.

Table 4
Main characteristics of dual-energy CT platforms of Philips Healthcare.

Model	IQon Spectral CT	Spectral CT 7500
DECT platform	Dual CT	Dual CT
kVp available	120 & 140	100, 120 & 140
Total filtration (eq mmAl)	6.9 mm*	6.9 mm*
mA range	from 10 to 1000	from 10 to 1000
TCM system used	DoseRight Z-DOM & 3D-DOM	DoseRight Z-DOM & 3D-DOM
Beam collimation range (mm)	from 7.5 to 40	from 7.5 to 80
Rotation time range (s)	from 0.27 to 2	from 0.27 to 1
Pitch range	from 0.07 to 1.5	from 0.07 to 1.7
Temporal resolution max (ms)	135	135
Cardiac gating	Yes	Yes
Raw data or images space	Raw data	Raw data
Reconstruction algorithm	Spectral 8 levels	Spectral 8 levels

* At 140 kVp.
Z-DOM: Axis dose modulation; 3D-DOM: Angular and longitudinal dose modulation; DECT: Dual-energy CT; DLSR: Deep learning spectral reconstruction; TCM: Tube current modulation.

For all systems, 32 cm and 50 cm scanning FOVs are available, with a native collimation of 0.625 mm. Images can be reconstructed using a display FOV of 5 to 50 cm, matrix size of 512^2 pixels and different algorithm generations: ASIR on Revolution GSI, ASIR-V on Revolution Frontier and on Revolution CT and Revolution Apex platforms. The new Deep Learning image reconstruction algorithm, TrueFidelity™, is available for the two latter platforms.

The various types of spectral images generated on GE DECT systems are depicted in Table 1.

2.3.3. Philips Healthcare

Philips Healthcare has chosen to use dual-layer detector technology (*i.e.*, NanoPanel prism detector) (Table 4). The two photon spectra are obtained simultaneously without any additional constraints compared to a conventional helical acquisition, except for certain tube voltage values. Indeed, only 80 and 100 kVp for the iQon and 80 kVp for the CT7500 are not validated for spectral imaging. It is therefore not necessary to define whether spectral reconstructions are desired, before acquisition.

Both machines have a z-flying focal spot and the beam collimations available are 40 mm for the iQon and 80 mm for the CT7500. Typical pitch factors range from 0.07 to 1.5 (1.65 for CT7500) for table travel speeds of 185 (600 for CT7500) mm/s. Cardiac gating can be prospective or retrospective and the temporal resolution can be as low as 135 ms. Tube current modulation is identical to conventional CT acquisition: Dose Right Index associated with Z-DOM or 3D-DOM modulation and electrocardiogram (ECG) in cardiac acquisitions.

The material decomposition process is performed in the raw data domain. Reconstruction slice thicknesses can vary from 0.67 to 1 cm on 50 cm FOV and 512^2 pixels matrix size. The spectral reconstruction algorithm is used for different reconstruction kernels.

The various types of spectral images generated on both Philips DECT systems are depicted in Table 1.

2.3.4. Siemens Healthineers

For Siemens Healthineers, two-photon spectra are obtained during the acquisition with two different dual-energy CT platforms (Table 5).

On the dual-source CT (DSCT) platform, image datasets are acquired with two X-Ray tube/detector pairs dephased by 95° for the Somatom Force and Somatom Drive. One X-ray tube uses a low kVp (70–100 kVp) and the other uses a high kVp with or without a tin filter (140 kVp or Sn150 kVp), resulting in better spectral separation than other platforms developed by this manufacturer. Different kVp pairs are available depending on the CT system, allowing adaptation to the patient's morphology or clinical indication for the CT examination. The use of two tubes, a low rotation time and smaller pitch factor means that cardiac gating CT scans can be performed with temporal resolutions of 66 to 75 ms. However, the detector array of the second tube is reduced to a width of 33 or 35 cm (50 cm for the first tube), limiting the acquisition and reconstruction FOV to 33 or 35 cm.

With split filter CT platform, one X-ray tube/detector pair with a 120 kVp (or 140 kVp) tube voltage is coupled with two filters to split the energy spectra into one low- (0.05-mm-thick gold filter) and one high-energy (0.6-mm-thick tin filter) spectra. Both the acquisition and reconstruction FOVs are 50 cm maximum. Rotation time ranges from 0.25 to 1 s/rot depending on the CT system but the pitch factor is limited to 0.25–0.45. Cardiac gating cannot be performed with this system. Temporal resolution ranges from 125 to 165 ms, depending on the system.

With DSCT platform, several beam collimations can be used whereas only one collimation is available with split filter CT. Also, the tube CareDose 4D current modulation system can be used for all split filter CT and DSCT systems. In addition, as the spectral images are obtained in the image domain, the iterative reconstruction algorithms ADMIRE or SAFIRE can be used for different reconstruction kernels and slice thicknesses ranging from 0.5 to 10 mm. The spectral images can be reconstructed with a 512^2 pixel matrix for the two platforms, and 768^2 and 1024^2 pixel matrix only for DSCT.

Table 5
Main characteristics of dual-energy CT platforms of Siemens Healthineers.

Model	Somatom Force	Somatom Drive	Edge+	Xcite	Xceed	GoTop
DECT platform	Dual-source CT	Dual-source CT	Split Filter CT	Split Filter CT	Split Filter CT	Split Filter CT
kVp available	70/Sn150; 80/Sn150; 90/Sn150; 100/Sn150; 80/140	80/Sn140; 100/Sn140; 80/140	120 kVp AuSn	120 or 140 kVp AuSn	120 or 140 kVp AuSn	120 or 140 kVp AuSn
Total filtration (eq mmAl)	5.7 mm*	6.8 mm**	6.8 mm**	5.7 mm *	5.7 mm*	5.5 mm***
mA range	40 to 2600 mA	40 to 1600 mA	20 to 800 mA	20 to 1200 mA	10 to 1300 mA	20 to 825 mA
TCM system used	CareDose 4D	CareDose 4D	CareDose 4D	CareDose 4D	CareDose 4D	CareDose 4D
Beam collimation range (mm)	from 38.4 to 57.6	from 24 to 38.4	38.4	38.4	38.4	38.4
Rotation time range (s)	from 0.25 to 1	from 0.28 to 1	from 0.28 to 1	from 0.3 to 1	from 0.25 to 1	from 0.33 to 1
Pitch range	from 0.2 to 1.2	from 0.2 to 1.2	from 0.25 to 0.45	from 0.25 to 0.45	from 0.25 to 0.45	from 0.25 to 0.45
Temporal resolution max (ms)	66	75	140	150	125	165
Cardiac gating	Yes	Yes	No	No	No	No
Raw data or images space	Images	Images	Images	Images	Images	Images
Reconstruction algorithm	ADMIRE	ADMIRE	ADMIRE	ADMIRE	ADMIRE	ADMIRE

* At 150 kVp, ** At 145 kVp and *** At 150 kVp.
ADMIRE: Advanced modeled iterative reconstruction; DECT: Dual-energy CT; TCM: Tube current modulation.

The different types of spectral images generated on the Siemens DECT systems are reported in Table 1.

2.3.5. Double helical acquisition

On certain CT systems, another technique is also used for dual-energy acquisitions. This technique consists of making a first helical acquisition with a low tube voltage, then a second one with high tube voltage (with or without additional filtration). Its use remains limited to reducing metallic artifacts, correcting beam-hardening or characterizing urinary lithiasis. Indeed, the long time between the beginning of the first acquisition and the end of the second does not allow this technique to be used with iodinated contrast product injection.

2.4. Assessment of spectral performance

Spectral images have quantitative capabilities of great clinical importance as they improve the detection and characterization of certain lesions and can help treatment decisions for patients [31,63-65]. These quantitative parameters must be accurate and reproducible. To assess the quality of spectral images on a single DECT platform or on several DECT platforms with different technologies, many metrics are used on both phantoms and patients.

On VMIs, classical metrics can be calculated from regions of interest (ROIs) positioned on inserts on a phantom or on tissues/lesions in patient images. From these ROIs, classical metrics such as HU values, image noise but also signal-to-noise ratio (SNR) and CNR can be calculated. In particular, these metrics make it possible to evaluate the variation in contrast of a material or tissue/lesion depending on the monoenergetic level. Furthermore, on the phantoms, to ensure the accuracy of the HUs calculated in the spectral images, metrics such as root-mean-square deviation or monochromatic bias are measured [66–73]. These can evaluate the difference between the HU value measured in a given insert and its theoretical value. These two metrics are also used to assess the accuracy of the iodine concentration on iodine maps [61,66-71,74,75]. The higher the accuracy of the HU and iodine, the better the spectral performance and the more relevant the clinical results. In addition, these metrics can also be used to ensure the relevance of electron density and effective Z maps, used particularly in radiotherapy departments [42,43,47,76].

New so-called advanced metrics have recently been developed to assess the quality of conventional CT images [77–79]. These metrics are beginning to be used to assess the quality of VMIs as they allow the assessment of other image characteristics [58-60,69,74,80-82]. Noise power spectrum (NPS) is used to evaluate the texture and amplitude of noise according to keV. Task-based transfer function (TTF) is used to evaluate the spatial resolution under near-clinical contrast and noise conditions. Thus, for inserts containing an iodine concentration, this will be calculated by taking into account the variations of noise and contrast (increase at low keV for both) as a function of keV. Finally, the detectability index calculated from a model observer can also be used to evaluate the detectability of a simulated lesion. This metric is similar to the CNR but has the advantage of taking into account the noise and its texture, the blur from the TTF and a visualization function that simulates the response of the human eye. This metric is very useful for determining the optimal monoenergetic level for detecting a lesion based on its size and composition, which is essential in clinical routine [58,59,69,74,80].

To evaluate all these metrics, it is essential to use suitable phantoms. For classical metrics, the phantoms must be composed of inserts of sufficient size and materials of similar composition/density to the tissue present in the spectral images. Thus, iodine inserts of different concentrations are used to assess the accuracy of HUs and iodine concentration. Furthermore, it is essential to know the

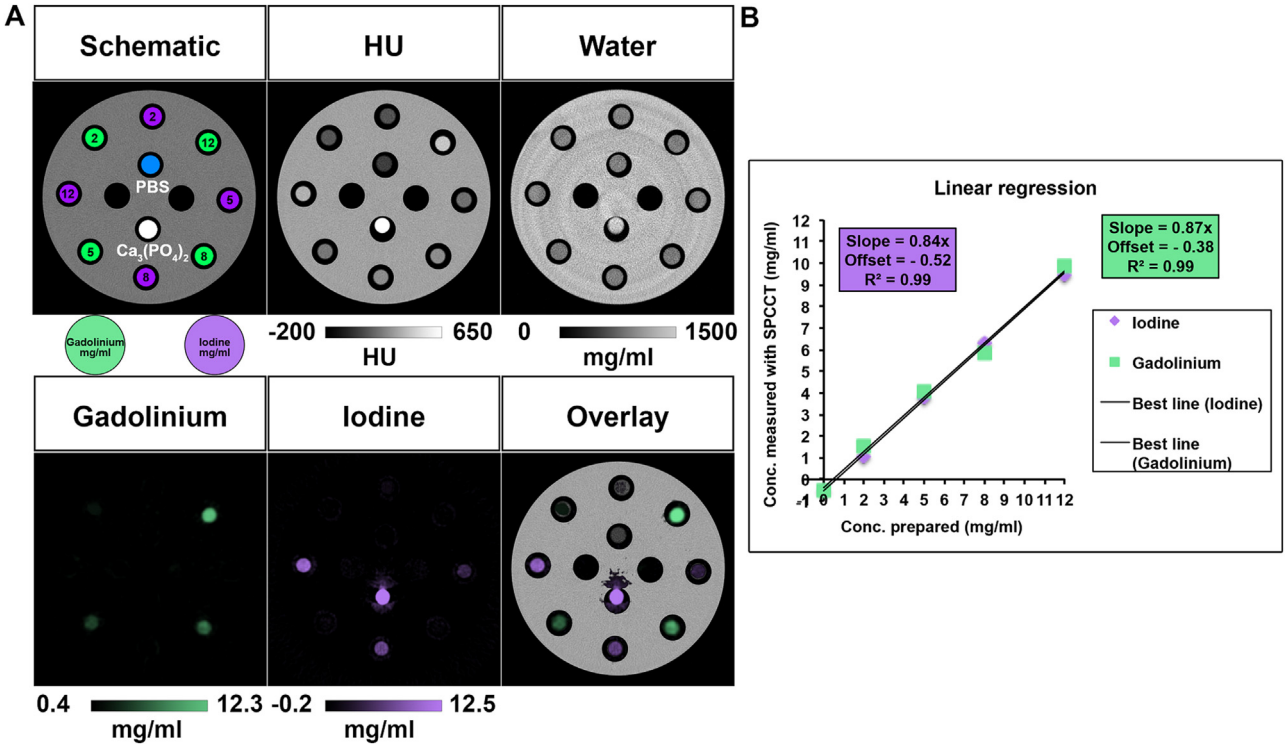


Fig. 3. Illustration of Color K-edge imaging capabilities enabled by the spectral photon-counting CT technology in a phantom with multiple materials.

A. Schematic drawing, spectral photon-counting CT (SPCCT) images and material decomposition images into water, iodine and gadolinium K-edge of a phantom containing tubes with increasing concentrations of contrast agents (2, 5, 8, and 12 mg/mL), with calcium phosphate and phosphate buffered saline tubes. While conventional image failed to provide specific imaging of each contrast agent and that iodine images failed to differentiate between iodine and calcium, gadolinium K-edge image showed specific differentiation of gadolinium tubes without cross-contamination with the advantage to be quantitative.

B, Comparison of actual and SPCCT measured contrast agent concentrations, showing a linear correlation (Image reprinted, with permission, from reference [93]).

variation of the linear attenuation coefficient and the theoretical HU value as a function of keV for each insert. There are many phantoms available for measuring these classical metrics [58-60,66-70,74,80,83]. However, these phantoms are not always suitable for evaluating advanced metrics. Indeed, the NPS must be measured in a phantom with a homogeneous cross-section, which is the case for most classical image quality phantoms but for those used to measure classical metrics. The TTF must be calculated on inserts of suitable sizes with a sufficiently large homogeneous area around the insert. Furthermore, for spectral images, it must be calculated on inserts similar to the clinical lesions studied (i.e., iodine or calcium inserts). However, to date, there are no phantoms on the market with sections that meet these different requirements simultaneously. Only the Mercury v4.0 (Gammex™ Technology) the phantom allows TTF calculation but only on a single iodine insert at 10 mg/ml [83,84].

It is therefore essential to assess spectral image quality to ensure that radiologists can make accurate clinical diagnoses if radiotherapy treatment is to be made more reliable. Several metrics exist to assess image quality. These require suitable phantoms and these are not always available on site. To ensure consistent performance over time, quality control of spectral images should be implemented [85,86].

3. Spectral photon counting CT technology

3.1. Principles

Spectral photon-counting CT (SPCCT) is a new, emerging technology in the field of spectral imaging [87,88]. It makes use of energy-resolving detectors, called photon-counting detectors (PCDs), recently integrated into clinical CT platforms [89,90]. PCDs are made of semi-conductive material which makes it possible to convert incoming photons directly into electrical charges which migrate into a counting (Application-specific integrated circuit, ASIC). The ASIC shapes a voltage pulse proportional to the incoming photon energy, and each photon can be differentiated in amplitude according to its energy [91]. The transmitted spectrum can thus be characterized into multiple energy bins as defined by their different energy levels. In comparison to dual-energy CT abilities, SPCCT has the potential to

Table 6
Main characteristics of current spectral photon-counting CT systems suitable for clinical imaging. Note that two of them are designed with small bore gantry for head (Samsumg Healthcare) and for extremities (MARS Bioimaging limited system) imaging and that 2 of them have been FDA-cleared (Siemens Healthineers and Samsumg Healthcare).

Manufacturer	CT plateforms	PCD materials	Geometry	Detector size at isocenter	Field-of-view	Energy thresholds	Current status
Canon Medical Systems	Aquilion ONE VISION	CdZT	Single source	0.342 mm	50 cm	5 available	Clinical prototype evaluation on going ; Not cleared or approved by the U.S. FDA or any other global regulator for commercial availability; Clinical trial pending
GE Healthcare	LightSpeed VCT CT Scanner	Silicon	Single source	0.250 mm	50 cm expected	8 available	Clinical prototype evaluation on going ; Not cleared or approved by the U.S. FDA or any other global regulator for commercial availability
MARS Bioimaging Limited (MBI)		CdZT	Single source	0.110 mm	11 cm	5 in “charge summing mode”	Not cleared or approved by the U.S. FDA or any other global regulator for commercial availability; Pre-clinical research; Clinical trial pending
Philips Healthcare	Philips iCT plateform	CdZT	Single source	0.274 mm	50 cm	5 in standard mode; 5 in HR modes	Clinical prototype evaluation on going; Not cleared or approved by the U.S. FDA or any other global regulator for commercial availability; Clinical trial and pre-clinical research in progress
Samsumg Healthcare	OmniTom Portable PCD Head CT	CdT	Single source	0.12 mm (HR); 0.4 mm (HR); 0.7 mm (standard)	25 cm	3 available	FDA-cleared in march 2022; Clinical trial pending
Siemens Healthineers	NAEOTOM Alpha	CdT	Dual-source	0.300 mm (standard); 0.150 mm (HR)	50 cm; 36 cm used for cardiac scans; 36 cm for high helical pitch scans	4 in standard mode; 2 in HR mode	FDA-cleared in september 2021; Pre-clinical and Clinical research on Human ; Commercially available

Parameters listed are based on the current status of the manufacturer’s development and are expected to evolve in a near future. Cd: Cadmium, Z: Zinc, T: Telluride.
FDA: Food and Drug Administration; PCD: Photon-counting detectors; U.S.: United States of America; HR: High-resolution mode.

provide more complete, accurate sampling of the energy dependence found in the CT images. Many advantages still in current development can be expected. However, it is worth mentioning that SPCCT opens up an extended approach to spectral imaging by first improving the energy separation between high and low energy photons [92]. This offers greater resolution of photoelectric and Compton contribution/absorption coefficients that will enhance the current known spectral capabilities such as virtual monochromatic images (VMI). The second benefit will be that additional materials can be added to the spectral decomposition of the images based on their K-edge energies (*i.e.*, the binding energy between the K-shell and the nucleus) [93–107]. This can be understood as a third unknown factor added to the equation by Alvarez and Macovsky [10] (Eq. 5).

$$\mu(E) = \alpha_P f_P(E) + \alpha_C f_c(E) \ + \alpha_{material} f_{material}(E) \quad (5)$$

where $f_{material}(E)$ is mathematical function that characterized photoelectric effect of the K-edge material and $\alpha_{material}$ is the photoelectric absorption coefficient of the material.

This approach, referred to as K-edge imaging, is a real breakthrough in CT post-processing and comes with the promise of being available in the next generation of clinical SPCCT systems. It mainly promises to overcome the limitations of dual-energy CT technology which cannot specifically or quantitatively separate different materials in the same voxel (or spatially co-registered), such as iodine and calcium (Fig. 3). These images will soon be offered to radiologists together with the conventional HU-image which is impossible with conventional CT or dual-energy CT. K-edge imaging is similar to the nuclear imaging twin modality of positron emission tomography-CT in which low-resolution functional information on 18F-fluorodeoxyglucose uptake is superimposed on high-resolution anatomical information, opening a completely new CT approach for functional, molecular or inflammation imaging and many other areas requiring exploration.

3.2. Technical aspects

The energy-resolving capabilities of PCD have many advantages over conventional energy-integrating CT detectors that include: (*i*), individual photon counting; (*ii*), individual photon energy discrimination; (*iii*), No electronic noise (threshold to discriminate between electronic noise and X-ray pulse); (*iiii*) Improved spatial resolution: the small charge cluster size and absence of electronic noise make it possible to use a smaller pixel size than with conventional scintillator and photodiode CT detectors; (*v*), improved energy weighting of the low-energy photons leading to higher CT attenuation and contrast within the tissue; and (*vi*), no dead space between detectors [89,107].

These technical aspects will bring new important features to clinical imaging that include: (*i*), higher spatial resolution: higher modulation transfer function (MTF) in the usual range 0–15 lp/cm and significant strength in the extension to 30 lp/cm; (*ii*), reduced noise at low dose since photon counting does not have a noise floor from electronics; (*iii*), reduced noise in the decomposition of two base materials from a greater number of energy bins detected and stored in the data; (*iv*), possibility of decomposing more than two base materials from multiple energy bins; (*v*), improved, ;more adaptable reconstruction contrast from multiple energy bins; and (*vi*), possibility to map K-edge materials (like gadolinium, gold or bismuth) with dynamic assignment in software.

3.3. Towards clinical imaging

Over the past five years the SPCCT field has made considerable progress with the implementation of PCD with high-count-rate capabilities in wide-bore CT platforms. So far, this shift has proved successful with two FDA-cleared systems (*i.e.*, one wide-bore for all applications) [108] and one small-bore for head imaging. Nevertheless, despite the various technical choices of the different manufacturers, many pre-clinical and clinical studies have provided evidence that SPCCT can be considered as the future of spectral CT imaging (Table 6)[109–117].

4. Conclusion

Spectral CT imaging is a constantly developing field which gained interest when dual-energy CT systems became implemented in clinical practice twenty years ago. Despite the different manufacturer's choices in terms of detection chain, X-ray source, reconstruction chain and other parameters, they all provide radiologists with the possibility of benefitting from the tissue's energy dependence via virtual monochromatic images and breaking down materials into water, iodine and other materials. Nevertheless, the spectral CT imaging field has not stopped evolving both in overcoming the limitations of dual-energy CT and exploring new approaches in CT imaging via new developments such as K-edge imaging in spectral photon-counting CT technology.

Declaration of Competing Interest

The authors declare that they have no known competing financial or personal relationships that could be viewed as influencing the work reported in this paper.

Acknowledgements

We wish to thank Teresa Sawyers, medical writer at the BESPIM, Nîmes University Hospital for her help in editing the manuscript. We also thank Anthony Thay and Christiana Balta, (clinical scientists at Canon Medical Systems), Hugo Pasquier (clinical scientist at GE Healthcare), Marjorie Villien (clinical scientist at Philips Healthcare) and Cédric Croisille (clinical scientist at Siemens Healthineers) who have reviewed and validated the Table and the part related to their DECT platforms.

Informed consent and patient details

The authors declare that this article does not contain any personal information that could lead to the identification of the patients.

Funding

This work did not receive any grant from funding agencies in the public, commercial, or not-for-profit sectors.

Contribution of authors

All authors attest that they meet the current International Committee of Medical Journal Editors (ICMJE) criteria for Authorship.

References

[1] Hounsfield GN. Computerized transverse axial scanning (tomography). 1. Description of system. Br J Radiol 1973;46:1016–22.
[2] Nishimaru E. The fundamental principle in X-ray CT scanner. Nihon Hoshasen Gijutsu Gakkai Zasshi 2015;71:1123–31.
[3] Meduri S, De Petri T, Modesto A, Moretti CA. Multislice CT: technical principles and clinical applications. Radiol Med 2002;103:143–57.
[4] McCollough CH, Leng S, Yu L, Fletcher JG. Dual- and multi-energy CT: principles, technical approaches, and clinical applications. Radiology 2015;276:637–53.
[5] Agostini A, Borgheresi A, Mari A, Floridi C, Bruno F, Carotti M, et al. Dual-energy CT: theoretical principles and clinical applications. Radiol Med 2019;124:1281–95.
[6] Lestra T, Mulé S, Millet I, Carsin-Vu A, Taourel P, Hoeffel C. Applications of dual energy computed tomography in abdominal imaging. Diagn Interv Imaging 2016;97:593–603.

[7] Coursey CA, Nelson RC, Boll DT, Paulson EK, Ho LM, Neville AM, et al. Dual-energy multidetector CT: how does it work, what can it tell us, and when can we use it in abdominopelvic imaging? Radiographics 2010;30:1037–55.
[8] Fornaro J, Leschka S, Hibbeln D, Butler A, Anderson N, Pache G, et al. Dual- and multi-energy CT: approach to functional imaging. Insights Imaging 2011;2:149–59.
[9] Kalender WA, Perman WH, Vetter JR, Klotz E. Evaluation of a prototype dual-energy computed tomographic apparatus. I. Phantom studies. Med Phys 1986;13:334–9.
[10] Alvarez RE, Macovski A. Energy-selective reconstructions in X-ray computerized tomography. Phys Med Biol 1976;21:733–44.
[11] Patino M, Prochowski A, Agrawal MD, Simeone FJ, Gupta R, Hahn PF, et al. Material separation using dual-energy CT: current and emerging applications. Radiographics 2016;36:1087–105.
[12] McCollough CH, Boedeker K, Cody D, Duan X, Flohr T, Halliburton SS, et al. Principles and applications of multienergy CT: report of AAPM task group 291. Med Phys 2020;47:e881–912.
[13] Albrecht MH, Trommer J, Wichmann JL, Scholtz JE, Martin SS, Lehnert T, et al. Comprehensive comparison of virtual monoenergetic and linearly blended reconstruction techniques in third-generation dual-source dual-energy computed tomography angiography of the thorax and abdomen. Invest Radiol 2016;51:582–90.
[14] Primak AN, Ramirez Giraldo JC, Liu X, Yu L, McCollough CH. Improved dual-energy material discrimination for dual-source CT by means of additional spectral filtration. Med Phys 2009;36:1359–69.
[15] Long Y, Fessler JA. Multi-material decomposition using statistical image reconstruction for spectral CT. IEEE Trans Med Imaging 2014;33:1614–26.
[16] Dong X, Niu T, Zhu L. Combined iterative reconstruction and image-domain decomposition for dual energy CT using total-variation regularization. Med Phys 2014;41:051909.
[17] Abdellatif W, Nugent JP, Alballa F, Murray N, Jalal S, Ali IT, et al. Dual energy computed tomography collagen material decomposition for detection of lumbar spine disc extrusion and sequestration: a comparative study with greyscale computed tomography. Can Assoc Radiol J 2022; doi: 10.1177/08465371221118886.
[18] Diekhoff T, Kiefer T, Stroux A, Pilhofer I, Juran R, Mews J, Blobel J, Tsuyuki M, Ackermann B, Hamm B, Hermann KG. Detection and characterization of crystal suspensions using single-source dual-energy computed tomography: a phantom model of crystal arthropathies. Invest Radiol 2015;50:255–60.
[19] Ren L, McCollough CH, Yu L. Three-material decomposition in multi-energy CT: impact of prior information on noise and bias. Proc SPIE Int Soc Opt Eng 2018;10573:105731G.
[20] Schwaiger BJ, Gersing AS, Hammel J, Mei K, Kopp FK, Kirschke JS, Rummeny EJ, Wörtler K, Baum T, Noël PB. Three-material decomposition with dual-layer spectral CT compared to MRI for the detection of bone marrow edema in patients with acute vertebral fractures. Skeletal Radiol 2018;47:1533–40.
[21] Cavallaro M, D'Angelo T, Albrecht MH, Yel I, Martin SS, Wichmann JL, et al. Comprehensive comparison of dual-energy computed tomography and magnetic resonance imaging for the assessment of bone marrow edema and fracture lines in acute vertebral fractures. Eur Radiol 2022;32:561–71.
[22] Si-Mohamed S, Dupuis N, Tatard-Leitman V, Rotzinger D, Boccalini S, Dion M, et al. Virtual versus true non-contrast dual-energy CT imaging for the diagnosis of aortic intramural hematoma. Eur Radiol 2019;29:6762–71.
[23] Jamali S, Michoux N, Coche E, Dragean CA. Virtual unenhanced phase with spectral dual-energy CT: is it an alternative to conventional true unenhanced phase for abdominal tissues? Diagn Interv Imaging 2019;100:503–11.
[24] Jungblut L, Abel F, Nakhostin D, Mergen V, Sartoretti T, Euler A, Frauenfelder T, Martini K Impact of photon-counting-detector-CT derived virtual-monoenergetic-images and iodine-maps on the diagnosis of pleural empyema. Diagn Interv Imaging 2022; doi: 10.1016/j.diii.2022.09.006.
[25] Wang Y, Zhou H, Hu P, Zhao J, Mao Y, Li Z, et al. Dual-energy computed tomography of cardiac changes in IgG4-related disease. Front Cardiovasc Med 2022;9:792531.
[26] Shin J, Yoon H, Cha YJ, Han K, Lee MJ, Kim MJ, et al. Liver stiffness and perfusion changes for hepatic sinusoidal obstruction syndrome in rabbit model. World J Gastroenterol 2020;26:706–16.
[27] Lador F, Hachulla AL, Hohn O, Plojoux J, Ronot M, Montet X, et al. Pulmonary perfusion changes as assessed by contrast-enhanced dual-energy computed tomography after endoscopic lung volume reduction by coils. Respiration 2016;92:404–13.
[28] Mohammadzadeh A, Farzaneh M, Zahedmehr A, Kiani R, Shakiba M, Borhani A, et al. Coronary CT angiography and dual-energy computed tomography in ischemic heart disease. Arch Iran Med 2019;22:376–83.
[29] Si-Mohamed S, Chebib N, Sigovan M, Zumbihl L, Turquier S, Boccalini S, et al. In vivo demonstration of pulmonary microvascular involvement in COVID-19 using dual-energy computed tomography. Eur Respir J 2020;56:2022608.
[30] Si-Mohamed S, Moreau-Triby C, Tylski P, Tatard-Leitman V, Wdowik Q, Boccalini S, et al. Head-to-head comparison of lung perfusion with dual-energy CT and SPECT-CT. Diagn Interv Imaging 2020;101:299–310.
[31] Si-Mohamed SA, Congi A, Ziegler A, Tomasevic D, Tatard-Leitman V, Broussaud T, et al. Early prediction of cardiac complications in acute myocarditis by means of extracellular volume quantification with the use of dual-energy computed tomography. JACC Cardiovasc Imaging 2021;14:2041–2.
[32] Si-Mohamed SA, Restier LM, Branchu A, Boccalini S, Congi A, Ziegler A, et al. Diagnostic performance of extracellular volume quantified by dual-layer dual-energy CT for detection of acute myocarditis. J Clin Med 2021;10:3286.
[33] Dubourg B, Dacher JN, Durand E, Caudron J, Bauer F, Bubenheim M, et al. Single-source dual energy CT to assess myocardial extracellular volume fraction in aortic stenosis before transcatheter aortic valve implantation (TAVI). Diagn Interv Imaging 2021;102:561–70.
[34] Boccalini S, Si-Mohamed S, Matzuzzi M, Tillier M, Rotzinger DC, Revel D, et al. Effect of contrast material injection protocol on first-pass myocardial perfusion assessed by dual-energy dual-layer computed tomography. Quant Imaging Med Surg 2022;12:3903–16.
[35] Cheraya G, Sharma S, Chhabra A. Dual energy CT in musculoskeletal applications beyond crystal imaging: bone marrow maps and metal artifact reduction. Skeletal Radiol 2022;51:1521–34.
[36] Baffour FI, Ferrero A, Aird GA, Powell GM, Adkins MC, Bekele DI, et al. Evolving role of dual-energy CT in the clinical workup of gout: a retrospective study. AJR Am J Roentgenol 2022;218:1041–50.
[37] Omoumi P, Becce F, Racine D, Ott JG, Andreisek G, Verdun FR. Dual-energy CT: basic principles, technical approaches, and applications in musculoskeletal imaging (Part 1). Semin Musculoskelet Radiol 2015;19:431–7.
[38] Primak AN, Fletcher JG, Vrtiska TJ, Dzyubak OP, Lieske JC, Jackson ME, et al. Non-invasive differentiation of uric acid versus non-uric acid kidney stones using dual-energy CT. Acad Radiol 2007;14:1441–7.
[39] Ascenti G, Siragusa C, Racchiusa S, Ielo I, Privitera G, Midili F, et al. Stone-targeted dual-energy CT: a new diagnostic approach to urinary calculosis. AJR Am J Roentgenol 2010;195:953–8.
[40] Boll DT, Patil NA, Paulson EK, Merkle EM, Simmons WN, Pierre SA, et al. Renal stone assessment with dual-energy multidetector CT and advanced postprocessing techniques: improved characterization of renal stone composition—pilot study. Radiology 2009;250:813–20.
[41] Leng S, Shiung M, Ai S, Qu M, Vrtiska TJ, Grant KL, et al. Feasibility of discriminating uric acid from non-uric acid renal stones using consecutive spatially registered low- and high-energy scans obtained on a conventional CT scanner. AJR Am J Roentgenol 2015;204:92–7.
[42] Kruis MF. Improving radiation physics, tumor visualisation, and treatment quantification in radiotherapy with spectral or dual-energy CT. J Appl Clin Med Phys 2022;23:e13468.
[43] van Elmpt W, Landry G, Das M, Verhaegen F. Dual energy CT in radiotherapy: current applications and future outlook. Radiother Oncol 2016;119:137–44.
[44] Bar E, Lalonde A, Royle G, Lu HM, Bouchard H. The potential of dual-energy CT to reduce proton beam range uncertainties. Med Phys 2017;44:2332–44.
[45] Landry G, Dorringer F, Si-Mohamed S, Douek P, Abascal J, Peyrin F, et al. Technical note: relative proton stopping power estimation from virtual monoenergetic images reconstructed from dual-layer computed tomography. Med Phys 2019;46:1821–8.
[46] Kretschmer M, Sabatino S, Heyden S, Loeffler W,Wagner M RT planning with dual energy CT. White paper Siemens 2013, https://www.radiologische-allianz.de/site/assets/files/1658/1210_whitepaper_dual_energy_final-6.pdf.
[47] Di Maso LD, Huang J, Bassetti MF, DeWerd LA, Miller JR. Investigating a novel split-filter dual-energy CT technique for improving pancreas tumor visibility for radiation therapy. J Appl Clin Med Phys 2018;19:676–83.
[48] Yamada S, Ueguchi T, Ogata T, Mizuno H, Ogihara R, Koizumi M, et al. Radiotherapy treatment planning with contrast-enhanced computed tomography: feasibility of dual-energy virtual unenhanced imaging for improved dose calculations. Radiat Oncol 2014;9:168.
[49] Rotzinger DC, Si-Mohamed SA, Yerly J, Boccalini S, Becce F, Boussel L, et al. Reduced-iodine-dose dual-energy coronary CT angiography: qualitative and quantitative comparison between virtual monochromatic and polychromatic CT images. Eur Radiol 2021;31:7132–42.
[50] Patino M, Parakh A, Lo GC, Agrawal M, Kambadakone AR, Oliveira GR, et al. Virtual monochromatic dual-energy aortoiliac CT angiography with reduced iodine dose: a prospective randomized study. AJR Am J Roentgenol 2019;212:467–74.
[51] D'Angelo T, Cicero G, Mazziotti S, Ascenti G, Albrecht MH, Martin SS, et al. Dual energy computed tomography virtual monoenergetic imaging: technique and clinical applications. Br J Radiol 2019;92:20180546.
[52] Lourenco PDM, Rawski R, Mohammed MF, Khosa F, Nicolaou S, McLaughlin P. Dual-energy CT iodine mapping and 40-keV monoenergetic applications in the diagnosis of Acute bowel ischemia. AJR Am J Roentgenol 2018;211:564–70.
[53] Agrawal MD, Pinho DF, Kulkarni NM, Hahn PF, Guimaraes AR, Sahani DV. Oncologic applications of dual-energy CT in the abdomen. Radiographics 2014;34:589–612.
[54] Boedeker K, Hayes M, Zhou J, Zhang R,Yu Z Deep learning spectral CT: faster, easier and more intelligent. White paper Canon 2019, https://my.medical.canon/publication/ct/Deep_Learning_Spectral_CT.
[55] Goo HW, Goo JM. Dual-energy CT: new horizon in medical imaging. Korean J Radiol 2017;18:555–69.
[56] Marin D, Boll DT, Mileto A, Nelson RC. State of the art: dual-energy CT of the abdomen. Radiology 2014;271:327–42.
[57] Siegel MJ, Kaza RK, Bolus DN, Boll DT, Rofsky NM, De Cecco CN, et al. White paper of the Society of Computed Body Tomography and Magnetic Resonance on dual-energy CT, Part 1: technology and terminology. J Comput Assist Tomogr 2016;40:841–5.
[58] Greffier J, Viry A, Barbotteau Y, Frandon J, Loisy M, de Oliveira F, et al. Phantom task-based image quality assessment of three generations of rapid kV-switching dual-energy CT systems on virtual monoenergetic images. Med Phys 2022;49:2233–44.
[59] Greffier J, Si-Mohamed S, Dabli D, de Forges H, Hamard A, Douek P, et al. Performance of four dual-energy CT platforms for abdominal imaging: a task-based image quality assessment based on phantom data. Eur Radiol 2021;31:5324–34.

[60] Greffier J, Frandon J, Hamard A, Teissier JM, Pasquier H, Beregi JP, et al. Impact of iterative reconstructions on image quality and detectability of focal liver lesions in low-energy monochromatic images. Phys Med 2020;77:36–42.
[61] Zhang D, Li X, Liu B. Objective characterization of GE discovery CT750 HD scanner: gemstone spectral imaging mode. Med Phys 2011;38:1178–88.
[62] Thibault JB,Utschig M Revolution apex with quantix^{TM} 160 - when power meets coverage. White Paper GE Healthcare 2020, https://www.gehealthcare.com/-/jssmedia/global/products/images/revolution-apex-platform/quantix_whitepaper_jb78157xx.pdf?rev=-1.
[63] Wu J, Lv Y, Wang N, Zhao Y, Zhang P, Liu Y, Chen A, Li J, Li X, Guo Y, Wu T, Liu A. The value of single-source dual-energy CT imaging for discriminating microsatellite instability from microsatellite stability human colorectal cancer. Eur Radiol 2019;29:3782–90.
[64] Deniffel D, Sauter A, Dangelmaier J, Fingerle A, Rummeny EJ, Pfeiffer D. Differentiating intrapulmonary metastases from different primary tumors via quantitative dual-energy CT based iodine concentration and conventional CT attenuation. Eur J Radiol 2019;111:6–13.
[65] Pfeiffer D, Parakh A, Patino M, Kambadakone A, Rummeny EJ, Sahani DV. Iodine material density images in dual-energy CT: quantification of contrast uptake and washout in HCC. Abdom Radiol 2018;43:3317–23.
[66] Sellerer T, Noel PB, Patino M, Parakh A, Ehn S, Zeiter S, et al. Dual-energy CT: a phantom comparison of different platforms for abdominal imaging. Eur Radiol 2018;28:2745–55.
[67] Dabli D, Frandon J, Belaouni A, Akessoul P, Addala T, Berny L, et al. Optimization of image quality and accuracy of low iodine concentration quantification as function of dose level and reconstruction algorithm for abdominal imaging using dual-source CT: a phantom study. Diagn Interv Imaging 2022;103:31–40.
[68] Dabli D, Frandon J, Hamard A, Belaouni A, Addala T, Beregi JP, et al. Optimization of image quality and accuracy of low iodine concentration quantification as function of kVp pairs for abdominal imaging using dual-source CT: a phantom study. Phys Med 2021;88:285–92.
[69] Greffier J, Si-Mohamed S, Guiu B, Frandon J, Loisy M, de Oliveira F, et al. Comparison of virtual monoenergetic imaging between a rapid kilovoltage switching dual-energy computed tomography with deep-learning and four dual-energy CTs with iterative reconstruction. Quant Imaging Med Surg 2022;12:1149–62.
[70] Jacobsen MC, Schellingerhout D, Wood CA, Tamm EP, Godoy MC, Sun J, et al. Inter manufacturer comparison of dual-energy CT iodine quantification and monochromatic attenuation: a phantom study. Radiology 2018;287:224–34.
[71] Washio H, Ohira S, Karino T, Nitta Y, Hayashi M, Miyazaki M, et al. Accuracy of auantification of iodine and Hounsfield unit values on virtual monochromatic imaging using dual-energy computed tomography: comparison of dual-layer computed tomography with fast kilovolt-switching computed tomography. J Comput Assist Tomogr 2018;42:965–71.
[72] Hua CH, Shapira N, Merchant TE, Klahr P, Yagil Y. Accuracy of electron density, effective atomic number, and iodine concentration determination with a dual-layer dual-energy computed tomography system. Med Phys 2018;45:2486–97.
[73] Sauter AP, Muenzel D, Dangelmaier J, Braren R, Pfeiffer F, Rummeny EJ, et al. Dual-layer spectral computed tomography: virtual non-contrast in comparison to true non-contrast images. Eur J Radiol 2018;104:108–14.
[74] Greffier J, Frandon J, Sadate A, Akessoul P, Belaouni A, Beregi JP, et al. Impact of four kVp combinations available in a dual-source CT on the spectral performance of abdominal imaging: a task-based image quality assessment on phantom data. J Appl Clin Med Phys 2021;22:243–54.
[75] Kim H, Goo JM, Kang CK, Chae KJ, Park CM. Comparison of iodine density measurement among dual-energy computed tomography scanners from 3 vendors. Invest Radiol 2018;53:321–7.
[76] Tatsugami F, Higaki T, Nakamura Y, Honda Y, Awai K. Dual-energy CT: minimal essentials for radiologists. Jpn J Radiol 2022;40:547–59.
[77] Verdun FR, Racine D, Ott JG, Tapiovaara MJ, Toroi P, Bochud FO, et al. Image quality in CT: from physical measurements to model observers. Phys Med 2015;31:823–43.
[78] Samei E, Bakalyar D, Boedeker KL, Brady S, Fan J, Leng S, et al. Performance evaluation of computed tomography systems: summary of AAPM Task Group 233. Med Phys 2019;46:e735–56.
[79] Greffier J, Barbotteau Y, Gardavaud F. iQMetrix-CT: new software for task-based image quality assessment of phantom CT images. Diagn Interv Imaging 2022;103:555–62.
[80] Greffier J, Dabli D, Hamard A, Akessoul P, Belaouni A, Beregi JP, et al. Impact of dose reduction and the use of an advanced model-based iterative reconstruction algorithm on spectral performance of a dual-source CT system: a task-based image quality assessment. Diagn Interv Imaging 2021;102:405–12.
[81] Papadakis AE, Damilakis J. The effect of tube focal spot size and acquisition mode on task-based image quality performance of a GE revolution HD dual energy CT scanner. Phys Med 2021;86:75–81.
[82] Masuda S, Sugisawa K, Minamishima K, Yamazaki A, Jinzaki M. Assessment of the image quality of virtual monochromatic spectral computed tomography images: a phantom study considering object contrast, radiation dose, and frequency characteristics. Radiol Phys Technol 2021;14:41–9.
[83] Cester D, Eberhard M, Alkadhi H, Euler A. Virtual monoenergetic images from dual-energy CT: systematic assessment of task-based image quality performance. Quant Imaging Med Surg 2022;12:726–41.
[84] Greffier J, Frandon J, Durand Q, Kammoun T, Loisy M, Beregi JP, et al. Contribution of an artificial intelligence deep-learning reconstruction algorithm for dose optimization in lumbar spine CT examination: a phantom study. Diagn Interv Imaging 2022; doi: 10.1016/j.diii.2022.08.004.
[85] Green CA, Solomon JB, Ruchala KJ, Samei E. Design and implementation of a practical quality control program for dual-energy CT. J Appl Clin Med Phys 2021;22:249–60.
[86] Nute JL, Jacobsen MC, Stefan W, Wei W, Cody DD. Development of a dual-energy computed tomography quality control program: characterization of scanner response and definition of relevant parameters for a fast-kVp switching dual-energy computed tomography system. Med Phys 2018;45:1444–58.
[87] Greffier J, Frandon J. Spectral photon-counting CT system: toward improved image quality performance in conventional and spectral CT imaging. Diagn Interv Imaging 2021;102:271–2.
[88] Si-Mohamed S, Bar-Ness D, Sigovan M, Cormode DP, Coulon P, Coche E, et al. Review of an initial experience with an experimental spectral photon-counting computed tomography system. Nucl Instrum Methods Phys Res 2017;873:27–35.
[89] Taguchi K, Iwanczyk JS. Vision 20/20: single photon counting x-ray detectors in medical imaging. Med Phys 2013;40:100901.
[90] da Silva J, Gronberg F, Cederstrom B, Persson M, Sjolin M, Alagic Z, et al. Resolution characterization of a silicon-based, photon-counting computed tomography prototype capable of patient scanning. J Med Imaging 2019;6:043502.
[91] Blevis I X-ray detectors for spectral photon-counting CT. In: Taguchi K, Blevis I, Iniewski K, editors Spectral, photon counting computed tomography: technology and applications. Boca Raton, Fla: CRC, 2020;179–91.
[92] Alvarez RE. Estimator for photon counting energy selective x-ray imaging with multibin pulse height analysis. Med Phys 2011;38:2324–34.
[93] Si-Mohamed S, Thivolet A, Bonnot PE, Bar-Ness D, Kepenekian V, Cormode DP, et al. Improved peritoneal cavity and abdominal organ imaging using a biphasic contrast agent protocol and spectral photon counting computed tomography K-edge imaging. Invest Radiol 2018;53:629–39.
[94] Si-Mohamed S, Bar-Ness D, Sigovan M, Tatard-Leitman V, Cormode DP, Naha PC, et al. Multicolour imaging with spectral photon-counting CT: a phantom study. Eur Radiol Exp 2018;2:34.
[95] de Vries A, Roessl E, Kneepkens E, Thran A, Brendel B, Martens G, et al. Quantitative spectral K-edge imaging in preclinical photon-counting x-ray computed tomography. Invest Radiol 2015;50:297–304.
[96] Roessl E, Brendel B, Engel KJ, Schlomka JP, Thran A, Proksa R. Sensitivity of photon-counting based K-edge imaging in X-ray computed tomography. IEEE Trans Med Imaging 2011;30:1678–90.
[97] Roessl E, Proksa R. K-edge imaging in X-ray computed tomography using multi-bin photon counting detectors. Phys Med Biol 2007;52:4679–96.
[98] Si-Mohamed SA, Sigovan M, Hsu JC, Tatard-Leitman V, Chalabreysse L, Naha PC, et al. In vivo molecular K-edge imaging of atherosclerotic plaque using photon-counting CT. Radiology 2021;300:98–107.
[99] Sigovan M, Si-Mohamed S, Bar-Ness D, Mitchell J, Langlois JB, Coulon P, et al. Feasibility of improving vascular imaging in the presence of metallic stents using spectral photon counting CT and K-edge imaging. Sci Rep 2019;9:19850.
[100] Si-Mohamed S, Cormode DP, Bar-Ness D, Sigovan M, Naha PC, Langlois JB, et al. Evaluation of spectral photon counting computed tomography K-edge imaging for determination of gold nanoparticle biodistribution in vivo. Nanoscale 2017;9:18246–57.
[101] Cormode DP, Roessl E, Thran A, Skajaa T, Gordon RE, Schlomka JP, et al. Atherosclerotic plaque composition: analysis with multicolor CT and targeted gold nanoparticles. Radiology 2010;256:774–82.
[102] Cormode DP, Si-Mohamed S, Bar-Ness D, Sigovan M, Naha PC, Balegamire J, et al. Multicolor spectral photon-counting computed tomography: in vivo dual contrast imaging with a high-count rate scanner. Sci Rep 2017;7:4784.
[103] Cassol F, Portal L, Graber-Bolis J, Perez-Ponce H, Dupont M, Kronland C, et al. K-edge imaging with the XPAD3 hybrid pixel detector, direct comparison of CdTe and Si sensors. Phys Med Biol 2015;60:5497–511.
[104] Si-Mohamed S, Tatard-Leitman V, Laugerette A, Sigovan M, Pfeiffer D, Rummeny EJ, et al. Spectral photon-counting computed tomography: in-vivo single-acquisition multi-phase liver imaging with a dual contrast agent protocol. Sci Rep 2019;9:8458.
[105] Riederer I, Bar-Ness D, Kimm MA, Si-Mohamed S, Noel PB, Rummeny EJ, et al. Liquid embolic agents in spectral X-ray photon-counting computed tomography using tantalum K-edge imaging. Sci Rep 2019;9:5268.
[106] Riederer I, Si-Mohamed S, Ehn S, Bar-Ness D, Noel PB, Fingerle AA, et al. Differentiation between blood and iodine in a bovine brain-Initial experience with spectral photon-counting computed tomography. PLoS One 2019;14:e0212679.
[107] Si-Mohamed SA, Miailhes J, Rodesch PA, Boccalini S, Lacombe H, Leitman V, et al. Spectral photon-counting CT technology in chest imaging. J Clin Med 2021;10.
[108] Rajendran K, Petersilka M, Henning A, Shanblatt ER, Schmidt B, Flohr TG, et al. First clinical photon-counting detector CT system: technical evaluation. Radiology 2022;303:130–8.
[109] Willemink MJ, Persson M, Pourmorteza A, Pelc NJ, Fleischmann D. Photon-counting CT: technical principles and clinical prospects. Radiology 2018;289:293–312.
[110] Boccalini S, Si-Mohamed S, Dessouky R, Sigovan M, Boussel L, Douek P. Feasibility of human vascular imaging of the neck with a large field-of-view spectral photon-counting CT system. Diagn Interv Imaging 2021;102:329–32.
[111] Boccalini S, Si-Mohamed SA, Lacombe H, Diaw A, Varasteh M, Rodesch PA, et al. First in-human results of computed tomography angiography for coronary stent assessment with a spectral photon counting computed tomography. Invest Radiol 2022;57:212–21.
[112] Si-Mohamed S, Boccalini S, Rodesch PA, Dessouky R, Lahoud E, Broussaud T, et al. Feasibility of lung imaging with a large field-of-view spectral photon-counting CT system. Diagn Interv Imaging 2021;102:305–12.

[113] Si-Mohamed SA, Boccalini S, Lacombe H, Diaw A, Varasteh M, Rodesch PA, et al. Coronary CT angiography with photon-counting CT: first-in-human results. Radiology 2022;303:303–13.
[114] Baffour FI, Huber NR, Ferrero A, Rajendran K, Glazebrook KN, Larson NB, et al. Photon-counting detector CT with deep learning noise reduction to detect multiple myeloma. Radiology 2022. doi: 10.1148/radiol.220311.
[115] van der Werf NR, Rodesch PA, Si-Mohamed S, van Hamersvelt RW, Greuter MJW, Leiner T, et al. Improved coronary calcium detection and quantification with low-dose full field-of-view photon-counting CT: a phantom study. Eur Radiol 2022;32:3447–57.
[116] van der Werf NR, Si-Mohamed S, Rodesch PA, van Hamersvelt RW, Greuter MJW, Boccalini S, et al. Coronary calcium scoring potential of large field-of-view spectral photon-counting CT: a phantom study. Eur Radiol 2022;32:152–62.
[117] Thivolet A, Si-Mohamed S, Bonnot PE, Blanchet C, Kepenekian V, Boussel L, et al. Spectral photon-counting CT imaging of colorectal peritoneal metastases: initial experience in rats. Sci Rep 2020;10:13394.